

Unconventional band splitting of CeSb in the devil's staircase transition

Tongrui Li^{1*}, Zhanfeng Liu^{1*}, Peng Li^{2*,†}, Yuzhe Wang^{1,3}, Zhisheng Zhao^{1,3}, Shiwu Su^{1,3},
Zhicheng Jiang¹, Yuhao Hong¹, Hui Tian¹, Xin Zheng¹, Yi Liu¹, Yilin Wang^{1,3}, Zhengtai Liu⁴,
Dawei Shen^{1,5}, Zhe Sun^{1†}, Yang Liu^{6†}, Juan Jiang^{1,3†}, Donglai Feng^{1,5}

¹ National Synchrotron Radiation Laboratory and School of Emerging Technology, University of Science and Technology of China, Hefei 230026, People's Republic of China

²Quantum Science Center of Guangdong–Hong Kong–Macao Greater Bay Area (Guangdong), Shenzhen 518045, China

³Hefei National Laboratory, University of Science and Technology of China, Hefei 230088, China

⁴Shanghai Synchrotron Radiation Facility, Shanghai Advanced Research Institute, Chinese Academy of Sciences, Shanghai, 201210, China

⁵School of Nuclear Science and Technology, and New Cornerstone Science Laboratory, University of Science and Technology of China, Hefei, 230026, China

⁶Center for Correlated Matter and School of Physics, Zhejiang University, Hangzhou 310058, China

*These authors contributed equally to this work.

[†]Emails: lipeng@quantumsc.cn; zsun@ustc.edu.cn; yangliuphys@zju.edu.cn; jjiangcindy@ustc.edu.cn

Abstract

The interplay between magnetism and electronic band structure is a central theme in condensed matter physics. CeSb, with its complex devil's staircase antiferromagnetic transition, offers a unique opportunity to explore this interplay. Using angle-resolved photoemission spectroscopy (ARPES), we investigate the electronic structure evolution across the devil's staircase transition. Upon entering the antiferromagnetic phase, we observe an intriguing band splitting of the electron pocket around the X point. The energy separation between the split bands changes abruptly with temperature, consistent with the characteristics of the first-order phase transition. However, their respective spectral weights behave gradually with temperature. Combined with our density functional theory (DFT) calculations, we suggest that this atypical behavior deviates from conventional magnetically induced band splitting and potentially arises from the intricate modulation of paramagnetic and antiferromagnetic layers within the devil's staircase transition. Our results provide insights into the complex relationship between electronic structure and magnetism in correlated electron systems.

Introduction

In strongly correlated systems, the interplay of multiple degrees of freedom, such as electronic charge, spin, and orbital, gives rise to complex and unexpected phenomena. Of particular interest are $4f$ electron systems, which exhibit a range of captivating phenomena, including heavy fermion superconductivity [1-3], the Kondo effect [4-7], and quantum criticality [7]. Understanding the magnetic mechanisms in such systems and unraveling their connections to electronic structures have become a focus of scientific investigation. The RePn (Re = La, Ce, Pr, Nd, Sm, Gd, Pn = Sb, Bi) family of compounds exhibit a wide range of interesting properties, including large magnetoresistance [8-11]

and topological properties in the paramagnetic (PM) phases [12-16]. Recently, the antiferromagnetic (AFM) phases of these compounds have attracted considerable attention [17-21] due to the intimate connection between magnetism and electronic structure. For instance, NdBi [17-19] and NdSb [20-22] exhibit intriguing Fermi-arc surface states and unconventional magnetic splitting in their antiferromagnetic phases related to the multi-q magnetic order. CeBi demonstrates unexpected band structure changes in the antiferromagnetic state[23].

CeSb stands out due to its exceptionally complex magnetic phase diagram, featuring more than seven distinct antiferroparamagnetic (AFP) phase transitions below its Néel temperature (T_N) of 17 K. This intricate sequence of transitions, known as the devil's staircase [24-26], includes a type-IA ($\uparrow\uparrow\downarrow\downarrow$) AFM structure below 8 K [27]. This structure consists of ferromagnetic aligned planes of Ce moments stacked antiferromagnetically along the c-axis ($\uparrow\uparrow\downarrow\downarrow$), where the arrows represent the magnetization direction within each plane. Previous ARPES studies on CeSb within the ‘devil's staircase’ regime have reported significant band renormalization of the hole bands near the Brillouin zone (BZ) center [28,29], initially attributed to band folding. Another ARPES study observed splitting-like electron bands at the BZ corner in the AFM phases [30], which was interpreted as Zeeman-type splitting caused by in-plane ferromagnetic exchange within a two-channel model. While neutron scattering studies have provided insights into the evolution of nonmagnetic Ce layers within the devil's staircase [24,26,31], direct electronic evidence supporting this model remain elusive.

In this letter, we use ARPES measurements and first-principles calculations to investigate the electronic band structure evolution of CeSb across the devil's staircase transition. We identify two distinct magnetic domains, differentiated by the electronic structure around the Γ point, and both present an unconventional band splitting at the X point. While the energy separation between the split bands remains largely temperature independent, their spectral weights show a pronounced temperature dependence. Combined with our DFT calculations, we propose that this splitting in the electron bands arises from the superposition of bands originating from both the nonmagnetic and magnetic Ce layers within the modulated devil's staircase magnetic structure.

Results and Discussion

The paramagnetic phase of CeSb crystallizes in the NaCl structure (#Space Group $Fm\bar{3}m$). The magnetic structure of the type-IA AFM is shown in Fig. 1a, with magnetic moments aligned along the c-axis. Experimentally, there are two distinct magnetic domains based on the two different cleavage planes: the *c*-domain, with out-of-plane moments and the *ab*-domain, with in-plane moments. Figure 1b illustrates the three-dimensional and surface-projected BZs of both the PM and AFM phases. Figure 1c shows the ARPES spectra along the high symmetry direction $\bar{\Gamma}\bar{X}_{PM}$ in the PM state, which agrees well with the calculated band structure in Fig. 1d and previous reports [32,33] (see Supplementary Figure 1 for more details of the Fermi surface). The energy distribution curve (EDC) at the \bar{X}_{PM} point presents a clear gap feature, indicating a topologically trivial PM phase [33]. While the overall Fermi surface topologies of the two antiferromagnetic domains appear similar (Figs. 1e and 1f), distinct differences emerge in the detailed band dispersions. Figures 1g and 1h show ARPES spectra along $\bar{\Gamma}\bar{X}_{PM}$ for the *c*-domain and *ab*-domain, respectively (cut directions indicated by black solid lines in Figs. 1e and 1f). The *c*-domain exhibits complex reconstructed bands near the $\bar{\Gamma}$ point, while the *ab*-domain shows fewer bands without clear electron-like features. These distinct characteristics are consistent with the previous report [28] (see Supplementary Figure 2 and Supplementary Figure 3 for further details).

To further investigate the electronic structure of the AFM phase, we conducted low-temperature ARPES measurements on both magnetic domains. Figure 2a presents the FS map of the *ab*-domain in the k_x - k_z plane measured using 28 eV photons (see Supplementary Figure 4 for the determination of different magnetic domains). The relationship between photon energy and k_z is shown in Fig. 2b. Figures 2c and 2d display the ARPES spectra and the corresponding second derivative images along cut 1 as indicated in Fig. 2a at 6 K ($T < T_N$) and 19.2 K ($T > T_N$), respectively. The parabolic electron band clearly splits in the AFM state, while the V-shaped electron band remains unaffected. On the contrary, along cut 2 (Figures 2e-2g), the V-shaped band exhibits splitting, whereas the parabolic band does not. Notably, a crossing-like feature shows up in Fig. 2e, likely arising from bulk bands as it disappears at a different photon energy (Fig. 2f). These observations indicate that the band splitting in the *ab*-domain exhibits C_2 symmetry. It is important to note that, although RePn system exhibits a strong kz broadening effect [11,12,20], making it difficult to detect a pure kz even with a single photon energy, the observed electronic structure that varies with photon energy reflects the intrinsic characteristics of the bulk bands. Figure 2h shows the FS of the *c*-domain, and Figs. 2i-k present ARPES spectra and second derivative images along cut 3 (indicated in Fig. 2h) at different photon energies and temperatures. Unlike the *ab*-domain, both the V-shaped and parabolic bands exhibit splitting in the *c*-domain, consistent with the C_4 symmetry. The weaker splitting of the V-shaped bands in the *c*-domain may be partially obscured by k_z -broadening arising from the finite escape depth of the photoelectrons (see Supplementary Figure 4 for the complete dataset).

To understand the origin of the band splitting in ARPES spectra, we performed DFT calculations for the AFM phase. The Hubbard U parameter was determined based on the energy position of the Ce $4f^0$ level. Figure 3a shows the resonant photoemission measurement at the Ce $4d \rightarrow 4f$ edge (122 eV) and reveals the $4f^0$ level at a binding energy between 2.6 eV and 3.2 eV. With f electrons treated as valence electrons, $U = 4.5$ eV and $J = 0.7$ eV were determined (see Supplementary Figure 5 for details). Figure 3b plots the band calculations for the AFM ground state (type-IA), with the energy position of the $4f^0$ level accurately reproduced. However, this calculation (Fig. 3d) does not reproduce the observed band splitting at the $\bar{M}(\bar{X}_{PM})$ point (Fig. 3c), where the experimentally measured splitting is approximately 0.11 eV. We also explored other antiferromagnetic configurations, but none of them can reproduce the ARPES measurements (see Supplementary Figure 6 for more magnetic configurations). Calculations for a ferromagnetic configuration (Fig. 3e) yield a Zeeman splitting of approximately 0.075 eV at the $\bar{M}(\bar{X}_{PM})$ point, smaller than the experimental value. Furthermore, the calculated band gap between the top of the valence bands and the bottom of the conduction bands at the $\bar{M}(\bar{X}_{PM})$ point in the ferromagnetic phase is ~ 0.17 eV, significantly larger than the experimental value. Thus, the possible ferromagnetic bands cannot reconcile with ARPES data. Interestingly, superimposing the calculated band structures of the paramagnetic and antiferromagnetic states (Fig. 3f) yields a splitting of approximately 0.12 eV between the upper and lower parabolic electron bands at the $\bar{M}(\bar{X}_{PM})$ point, in close agreement with the experimental value. Figures 3g, h, and i show the superposition of the calculated results (from Figures 3d, e, and f) and the experimental results (from Figures 3c) respectively. It is evident that the calculations in Figure 3i align well with the experimental data. This suggests that the observed splitting may arise from a superposition of paramagnetic and antiferromagnetic contributions. We summarize our findings in the schematic diagram shown in Supplementary Figure 7. It is worth noting that we employ the superposition method to provide a

proposal, as this approach better aligns with the experimental results. However, this superposition approach may not fully capture the underlying physics. The devil's staircase implies a complex spatial modulation of magnetic order, with potentially sharp interfaces between paramagnetic and antiferromagnetic regions, thus the temperature evolution of the band splitting would give more spectroscopic evidences.

Due to the use of vacuum ultraviolet light, the electron escape depth is limited and cannot effectively reach a significant depth. To better investigate the temperature evolution of the electronic structure of the devil's staircase transition, we will focus on exploring the temperature dependent experiment in the *ab* domain. Figure 4a shows ARPES spectra along cut 2 (Fig. 2a) for sample #1, and Fig. 4c shows similar data for sample #2 measured with a He lamp (21.2 eV). Both datasets reveal a splitting of the V-shaped electron band in the AFM phases, similar to previous reports [30]. The inner and outer bands are indicated by arrows in Figs. 4a and 4c, and are also evident in the momentum distribution curve (MDC) at E_F . Figs. 4b and 4d show EDCs extracted at the \bar{X}_{PM} point, fitted with two peaks (see Supplementary Figure 8 for fitting details). Below 17 K, two distinct peaks are observed, corresponding to the inner (blue dots) and outer (red dots) branches of the split band. As the temperature decreases, the peak position gradually shifts toward lower energy levels, resembling the phenomenon observed in CeBi [35], this behavior may be associated with the hybridization of *f* electrons and conduction electrons near the Fermi level. In addition, the spectral weight of the inner band gradually increases, while that of the outer band gradually diminishes. This temperature dependence correlates with the evolution of the devil's staircase, as shown in Fig. 4e, where the fraction of nonmagnetic Ce layers (gray dots) decreases with decreasing temperature, as determined by neutron scattering [24,26,31]. This suggests a possible connection between the observed band splitting and the presence of both magnetic and nonmagnetic Ce layers within the devil's staircase structure. Additionally, we attempted to calculate the electronic structure in intermediate magnetic configurations, such as the AFP1 state; however, we were unable to obtain the non-magnetic layer of Ce in the DFT calculations.

We quantified the temperature dependence of the outer band intensity by calculating the ratio $I_{outer} = outer / (inner + outer)$, where *inner* and *outer* are the intensities of the inner and outer peaks in the EDCs, respectively. Figure 4f shows I_{outer} for three different samples (#1, #2, and #3; see Supplementary Figure 9 for additional data of #3) alongside the temperature-dependent fraction of nonmagnetic Ce layers, I_{PM} , within the devil's staircase structure. The close agreement between I_{outer} and the I_{PM} suggests that the outer band originate from the nonmagnetic Ce layers. Remarkably, the energy separation between the inner and outer bands remains constant at approximately 0.1 eV below 17 K, as shown in Fig. 4g. These observations contrast with the behavior of typical magnetically induced band splitting, such as that observed in EuB₆ [36], where the splitting increases with decreasing temperature. However, this difference does not definitively rule out a magnetic origin for the splitting in CeSb, as the underlying mechanisms may be different. The observed temperature-dependent spectral weight transfer between the inner and outer bands is consistent with the changing fraction of magnetic and nonmagnetic Ce layers within the devil's staircase structure [37,38]. The residual intensity of the outer band below 8 K, where the devil's staircase model predicts only magnetic Ce layers, likely arises from phase fluctuations of the magnetic structure. This is because the lowest experimentally measured temperature is quite close to the phase transition temperature. Our data strongly suggest that the apparent band splitting in CeSb arises from the coexistence of paramagnetic and antiferromagnetic states, providing direct

spectroscopic evidence for the devil's staircase picture.

Conclusions

In summary, our combined ARPES and DFT + U study provides insights into the electronic structure of CeSb across the devil's staircase transition. The apparent band splitting observed at the \bar{X}_{PM} point in antiferromagnetic phase arises from the coexistence of paramagnetic and AFM states, reflecting the complex magnetic structure of CeSb. The temperature-dependent spectra weight transfer between the split bands can be well explained by the changing fraction of magnetic and nonmagnetic Ce layers within the devil's staircase magnetic structures. Our results provide direct spectroscopic evidence of the existence and evolution of the nonmagnetic Ce layers, offering a deeper understanding of the unusual electronic properties of this material.

Methods

Single crystals of CeSb were synthesized using the indium flux method with a molar ratio of Ce: Sb: Sn of 1: 1: 20. The starting materials were weighted and loaded in alumina crucibles, which were then sealed in an evacuated quartz tube and heated to 1150 °C before being cooled down to 800 °C. Finally, the samples were separated from the indium in a centrifuge. The typical crystal size was $4 \times 4 \times 4$ mm.

ARPES measurements were performed at beamline 03U of the Shanghai Synchrotron Radiation Facility (SSRF) in China. The ultra-high vacuum measurement was maintained below 8×10^{-11} Torr, and data were recorded using a Scienta DA30 analyzer. The total convolved energy and angle resolutions were 10 meV and 0.2°, respectively. The fresh surface for ARPES measurements was obtained by cleaving the CeSb samples in-situ along its natural cleavage plane.

Bulk electronic structure calculations were performed using density functional theory (DFT) with a plane wave basis projected augmented wave method [39], as implemented in the Vienna *ab-initio* simulation package (VASP) [40]. To address the overestimation of bandwidth by the PBE functional, we slightly increased the lattice constant by a factor of 1.08, following the method outlined in Ref. [20]. This adjustment ensured that no band inversion occurs at the X point in the paramagnetic state. The generalized gradient approximation of Perdew-Burke-Ernzerhof (PBE) [41] was used as the exchange-correlation potential. A tight binding model based on Wannier functions [42,43] was constructed to reproduce the spectral functions with the selection of Ce *d* and Sb *p* orbitals in the paramagnetic state. The spectrum and Fermi surfaces were calculated using surface Green's function methods [44,45], as implemented in WannierTools [46]. The 4f electrons were treated as valence electrons and spin-orbit coupling was included in the antiferromagnetic state. The energy cutoff was set to 300 eV and a $9 \times 9 \times 7$ Γ -centered k-mesh was employed in the calculation. $U = 4.5$ eV and $J = 0.7$ eV were used for our DFT+U+SOC calculations in the AFM phase, following the method of Liechtenstein *et al* [47], which matched well with the energy position of the $4f^0$ in resonance ARPES measurements. Fermi levels were shifted up by 180 meV to align with the ARPES spectra.

Data availability

The data that support the findings of this study are available from the corresponding authors upon request.

Reference

- [1] Steglich, F. et al. Superconductivity in the Presence of Strong Pauli Paramagnetism: CeCu_2Si_2 , *Phys. Rev. Lett.* **43**, 1892 (1979).
- [2] Singley, E. J., Basov, D. N., Bauer, E. D. & Maple, M. B. Optical conductivity of the heavy fermion superconductor CeCoIn_5 , *Phys. Rev. B* **65**, 161101(R) (2002).
- [3] Shishido, H. et al. Fermi surface, magnetic and superconducting properties of LaRhIn_5 and CeTiIn_5 (T: Co, Rh and Ir), *J. Phys. Soc. Jpn.* **71**, 162 (2002).
- [4] Coleman, P. & Nevidomskyy, A. H. Frustration and the Kondo effect in heavy fermion materials, *J. Low. Temp. Phys.* **161**, 182 (2010).
- [5] Nakatsuji, S. et al. Intersite Coupling Effects in a Kondo Lattice, *Phys. Rev. Lett.* **89**, 106402 (2002).
- [6] Dzero, M., Sun, K., Galitski, V. & Coleman, P. Topological Kondo Insulators, *Phys. Rev. Lett.* **104**, 106408 (2010).
- [7] Aynajian, P. et al. Visualizing heavy fermions emerging in a quantum critical Kondo lattice, *Nature* **486**, 201 (2012).
- [8] Jiang, J. et al. Observation of topological surface states and strong electron/hole imbalance in extreme magnetoresistance compound LaBi , *Phys. Rev. Materials* **2**, 024201 (2018).
- [9] Guo, P.-J. et al. Charge compensation in extremely large magnetoresistance materials LaSb and LaBi revealed by first-principles calculations, *Phys. Rev. B* **93**, 235142 (2016).
- [10] Ye, L., Suzuki, T., Wicker, C. R. & Checkelsky, J. G. Extreme magnetoresistance in magnetic rare-earth monpnictides, *Phys. Rev. B* **97**, 081108(2018).
- [11] Wu, Z.-Z. et al. Probing the origin of extreme magnetoresistance in Pr/Sm mon-antimonides/bismuthides, *Phys. Rev. B* **99**, 035158 (2019).
- [12] Niu, X.-H. et al. Presence of exotic electronic surface states in LaBi and LaSb , *Phys. Rev. B* **94**, 165163 (2016).
- [13] Duan, X. et al. Tunable electronic structure and topological properties of LnPn ($\text{Ln}=\text{Ce}, \text{Pr}, \text{Sm}, \text{Gd}, \text{Yb}$; $\text{Pn}=\text{Sb}, \text{Bi}$), *Communications Physics* **1**, 71 (2018).
- [14] Nayak, J. et al. Multiple Dirac cones at the surface of the topological metal LaBi , *Nat. Commun.* **8**, 13942 (2017).
- [15] Li, P. et al. Tunable electronic structure and surface states in rare-earth monobismuthides with partially filled f shell, *Phys. Rev. B* **98**, 085103 (2018).
- [16] Kuroda, K. et al. Experimental Determination of the Topological Phase Diagram in Cerium Monopnictides, *Phys. Rev. Lett.* **120**, 086402 (2018).
- [17] Schrunck, B. et al. Emergence of Fermi arcs due to magnetic splitting in an antiferromagnet, *Nature* **603**, 610–615 (2022).
- [18] Wang, L.-L. et al. Unconventional surface state pairs in a high-symmetry lattice with anti-ferromagnetic band-folding, *Communications Physics* **78** (2023).
- [19] Honma, A. et al. Antiferromagnetic topological insulator with selectively gapped Dirac cones, *Nat. Commun.* **14** 7396 (2023).
- [20] Li, P. et al. Origin of the exotic electronic states in antiferromagnetic NdSb , *npj Quantum Materials* **8**, 22 (2023).

- [21] Honma, A. et al. Unusual surface states associated with PT-symmetry breaking and antiferromagnetic band folding in NdSb, *Phys. Rev. B* **108**, 115118 (2023).
- [22] Kushnirenko, Y. et al. Rare-earth mononictides: Family of antiferromagnets hosting magnetic Fermi arcs, *Phys. Rev. B* **106**, 115112 (2022).
- [23] Kushnirenko, Y. et al. Unexpected band structure changes within the higher-temperature antiferromagnetic state of CeBi, *Communications Materials* **5**, 245 (2024).
- [24] Rossat-Mignod, J. et al. Phase diagram and magnetic structures of CeSb, *Phys. Rev. B* **16**, 440 (1977).
- [25] Boehm, J. von & Bak, P. Devil's Stairs and Commensurate-Commensurate Transitions in CeSb, *Phys. Rev. Lett* **42**, 122 (1979).
- [26] Lebech, B. Neutron diffraction studies of the modulated magnetic structures of CeSb and Nd metal (invited), *Journal of Applied Physics* **52**, 2019 (1981).
- [27] Hålg, B. & Furrer, A. Anisotropic exchange and spin dynamics in the type-I (-IA) antiferromagnets CeAs, CeSb, and USB: A neutron study, *Phys. Rev. B* **34**, 6258(1986).
- [28] Kuroda, K. et al. Devil's staircase transition of the electronic structures in CeSb, *Nat Commun.* **11**, 2888 (2020).
- [29] Arai, Y. et al. Multipole polaron in the devil's staircase of CeSb, *Nat. Mater.* **21**, 410–415 (2022).
- [30] Jang, S. et al. Direct visualization of coexisting channels of interaction in CeSb, *Sci. Adv.* **5**, eaat7158(2019).
- [31] Rossat-Mignod, J. et al. Neutron and magnetization studies of CeSb and CeSb_{1-x}Te_x solid solutions, *Journal of Magnetism and Magnetic Materials* **52** 111-121 (1985)
- [32] Wu, Y. et al. Electronic structure of RSb (R=Y, Ce, Gd, Dy, Ho, Tm, Lu) studied by angle-resolved photoemission spectroscopy, *Phys. Rev. B* **96**, 035134 (2017).
- [33] Oinuma, H. et al. Three-dimensional band structure of LaSb and CeSb: Absence of band inversion, *Phys. Rev. B* **96**, 041120(R) (2017).
- [34] Yuan, L.-D. et al. Giant momentum-dependent spin splitting in centrosymmetric low-Z antiferromagnets, *Phys. Rev. B* **102**, 014422 (2020).
- [35] Li, P. et al. Large Fermi surface expansion through anisotropic mixing of conduction and f electrons in the semimetallic Kondo lattice CeBi, *Phys. Rev. B* **100**, 155110 (2019).
- [36] Liu, W. L. et al. Spontaneous Ferromagnetism Induced Topological Transition in EuB₆, *Phys. Rev. Lett.* **129**, 166402 (2022)
- [37] Siemann, R. & Cooper, B. R. Planar Coupling Mechanism Explaining Anomalous Magnetic Structures in Cerium and Actinide Intermetallics, *Phys. Rev. Lett.* **44**, 1015 (1980).
- [38] Kioussis, N., Cooper, B. R. & Banerjee, A. Mechanism for the occurrence of paramagnetic planes within magnetically ordered cerium systems, *Phys. Rev. B* **38**, 9132(1988).
- [39] Blöchl, P. Projector augmented-wave method. *Phys. Rev. B* **50**, 17953 (1994)
- [40] Kresse, G. & Furthmüller, J. Efficient iterative schemes for ab initio total-energy calculations using a plane-wave basis set, *Phys. Rev. B* **54**, 11169 (1996)
- [41] Perdew, J. P., Burke, K. & Ernzerhof, M. Generalized Gradient Approximation Made Simple, *Phys. Rev. Lett.* **77**, 3865 (1996)
- [42] Marzari, N. & Vanderbilt, D. Maximally localized generalized Wannier functions for composite energy bands, *Phys. Rev. B* **56**, 12847 (1997)

- [43] Souza, I., Marzari, N. & Vanderbilt, D. Maximally localized Wannier functions for entangled energy bands, *Phys. Rev. B* **65**, 035109 (2001)
- [44] Sancho, M. P. L., Sancho, J. M. L. & Rubio, J. Quick iterative scheme for the calculation of transfer matrices: Application to Mo (100), *J. Phys. F Met. Phys.* **14**, 1205 (1984).
- [45] Sancho, M. P. L., Sancho, J. M. L., Sancho, J. M. L. & Rubio, J. Highly convergent schemes for the calculation of bulk and surface Green-functions, *J. Phys. F: Met. Phys.* **15**, 851 (1985)
- [46] Wu, Q.-S. et al. WannierTools: An open-source software package for novel topological materials, *Comput. Phys. Commun.* **224**, 405 (2018)
- [47] Liechtenstein, A. I., Anisimov, V. I. & Zaanen, J. Density-functional theory and strong interactions: Orbital ordering in Mott-Hubbard insulators, *Phys. Rev. B* **52**, R5467 (1995).

Acknowledgments

This work is supported by the National Key R&D Program of China (Grant No. 2023YFA1406304 (J. J), No. 2022YFA1402200 (Y. L)), the National Natural Science Foundation of China (Grant No. 12174362 (J. J), No. 11790312 (D. L. F), No. 92065202 (J. J)), the Postdoctoral Fellowship Program of CPSF(GZC20232530) (Z. F. L), the Innovation Program for Quantum Science and Technology (No. 2021ZD0302803 (D. L. F)) and the New Cornerstone Science Foundation (D. L. F). Part of this research used Beamline 03U of the Shanghai Synchrotron Radiation Facility, which is supported by ME2 project under contract no. 11227902 from National Natural Science Foundation of China.

Author Contributions

T.R.L., P.L. and Z.F.L. contribute equally to this work. P.L. and J.J. conceived the experiments. T.R.L., P.L. and J.J. carried out ARPES measurements with the assistance of Z.C.J., Yi. L., Z.S., Z.T.L. and D.W.S., T.R.L. performed the DFT calculations under the supervision of Y.L.W., Z.F.L. and P.L. synthesized and characterized bulk single crystals. Y.Z.W., Z.S.Z., S.W.S., Y.H.H., H.T., X.Z. contributed to measurements and data analysis. T.R.L., P.L., Z.S., Yang. L., J.J. and D.L.F. wrote the manuscript. All authors contributed to the scientific planning and discussions.

Competing interests

The authors declare no competing interests. Dawei Shen is an Editorial Board Member for Communications Materials and was not involved in the editorial review of, or the decision to publish, this Article.

Additional information

Supplementary information The online version contains supplementary material available at [xxxx](#).

Correspondence and requests for materials should be addressed to Juan Jiang or Peng Li.

Reprints and permissions information is available at <http://www.nature.com/reprints>

Publisher's note Springer Nature remains neutral with regard to jurisdictional claims in published maps and institutional affiliations.

Open Access This article is licensed under a Creative Commons Attribution 4.0 International License, which permits use, sharing, adaptation, distribution and reproduction in any medium or format, as long as you give appropriate credit to the original author(s) and the source, provide a link to the Creative Commons licence, and indicate if changes were made. The images or other third party material in this article are included in the article's Creative Commons licence, unless indicated otherwise in a credit line to the material. If material is not included in the article's Creative Commons licence and your intended use is not permitted by statutory regulation or exceeds the permitted use, you will need to obtain permission directly from the copyright holder. To view a copy of this licence, visit <http://creativecommons.org/licenses/by/4.0/>.

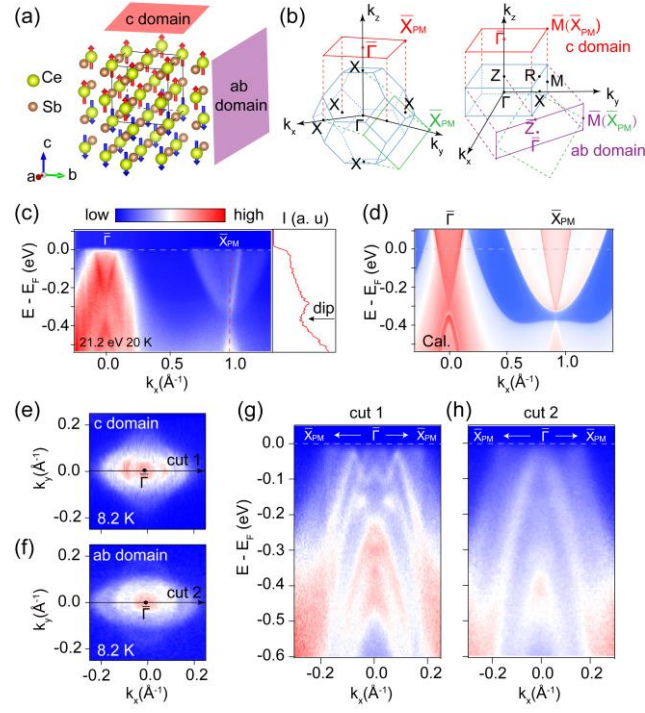


Fig. 1 Electronic structure of paramagnetic state and two magnetic domains of the antiferromagnetic ground state near $\bar{\Gamma}$. (a) Arrangement of magnetic moments of the type-IA antiferromagnetic structure, illustrating two possible magnetic domains: the *c*-domain and the *ab*-domain. (b) Brillouin zones of the paramagnetic phase and the type-IA antiferromagnetic phase. (c) ARPES intensity along $\bar{\Gamma}\bar{X}_{PM}$ in the paramagnetic phase. The EDC obtained along the red dashed line is plotted on the right side, revealing a distinct band gap. (d) Calculated band structure along $\bar{\Gamma}\bar{X}_{PM}$ in the paramagnetic phase. (e) The Fermi surface map of the *c*-domain near the $\bar{\Gamma}$ point. (f) The Fermi surface map of the *ab*-domain near the $\bar{\Gamma}$ point. (g, h) ARPES intensity plots along $\bar{\Gamma}\bar{X}_{PM}$ of cut 1 in (e) and cut 2 in (f), respectively.

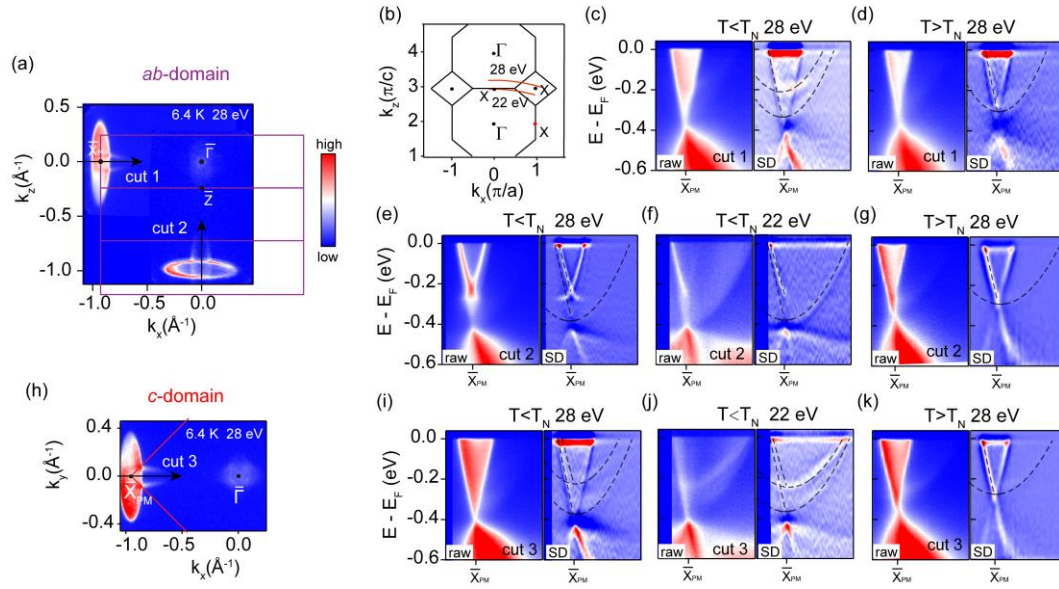


Fig. 2 Observation of splitting-like electron bands in *ab*- and *c*-domains. (a) Fermi surface map of the *ab*-domain measured using 28 eV photons at $T = 6.4$ K. (b) Relationship between photon energy and k_z in the k_z - k_x plane. (c, d) ARPES spectra along $\bar{\Gamma}\bar{X}_{PM}$ of cut 1 in (a) and the corresponding second derivative images, measured using 28 eV photons at $T = 6$ K and 19.2 K, respectively. (e, f, g) ARPES spectra along $\bar{\Gamma}\bar{X}_{PM}$ of cut 2 in (a) and the corresponding second derivative spectra, measured at 6.4 K with 28 eV and 22 eV photons, and 19.2 K with 28 eV photons, respectively. (h) Fermi surface map of the *c*-domain at 6.4 K with 28 eV photons. (i, j, k) ARPES spectra along $\bar{\Gamma}\bar{X}_{PM}$ of cut 3 in (h) and the corresponding second derivative spectra, measured at 8.1 K with 28 eV photons, 6.6 K with 22 eV photons, and 19.2 K with 28 eV photons, respectively.

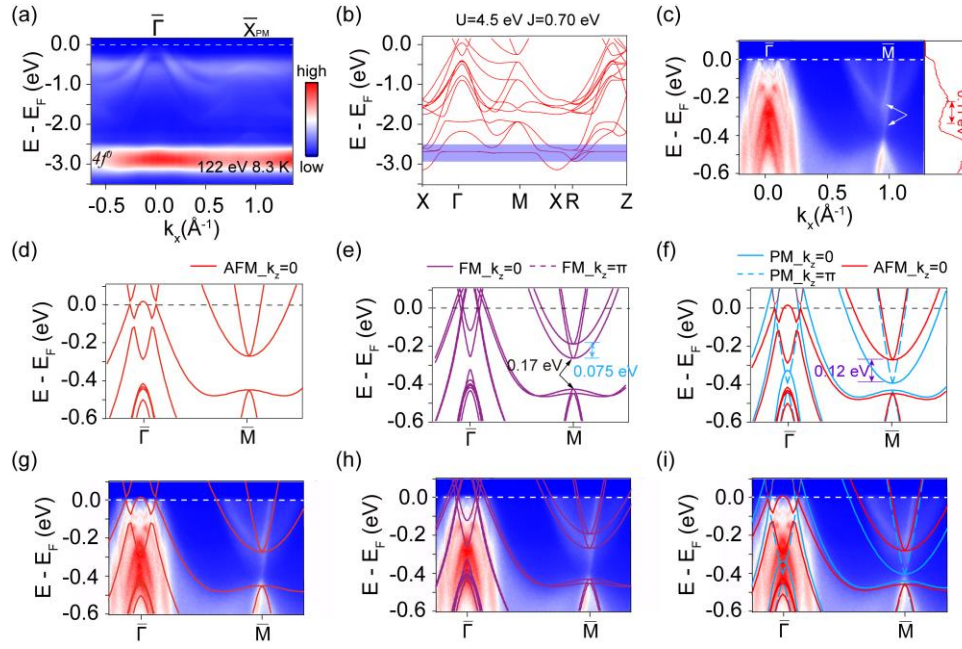


Fig. 3 Identification of paramagnetic and antiferromagnetic layers using DFT + U calculations. **(a)** Ce $4f^0$ energy level determined from resonant ARPES measurements using 122 eV photons, located around 2.8 eV below the Fermi level. **(b)** Values of the Hubbard U and Hund's coupling J parameters for the DFT+ U calculations of the antiferromagnetic ground phase. **(c)** ARPES spectra of the c -domain at 8.2 K. **(d)** Calculated band structure for the type-IA AFM phase. **(e)** Calculated band structure for the ferromagnetic phase. **(f)** Superimposed DFT calculations of the type-IA AFM and PM phases. The color scale represents the intensity of ARPES spectra. **(g, h, i)** ARPES spectra overlapped with DFT calculations in **(d, e, f)**, respectively.

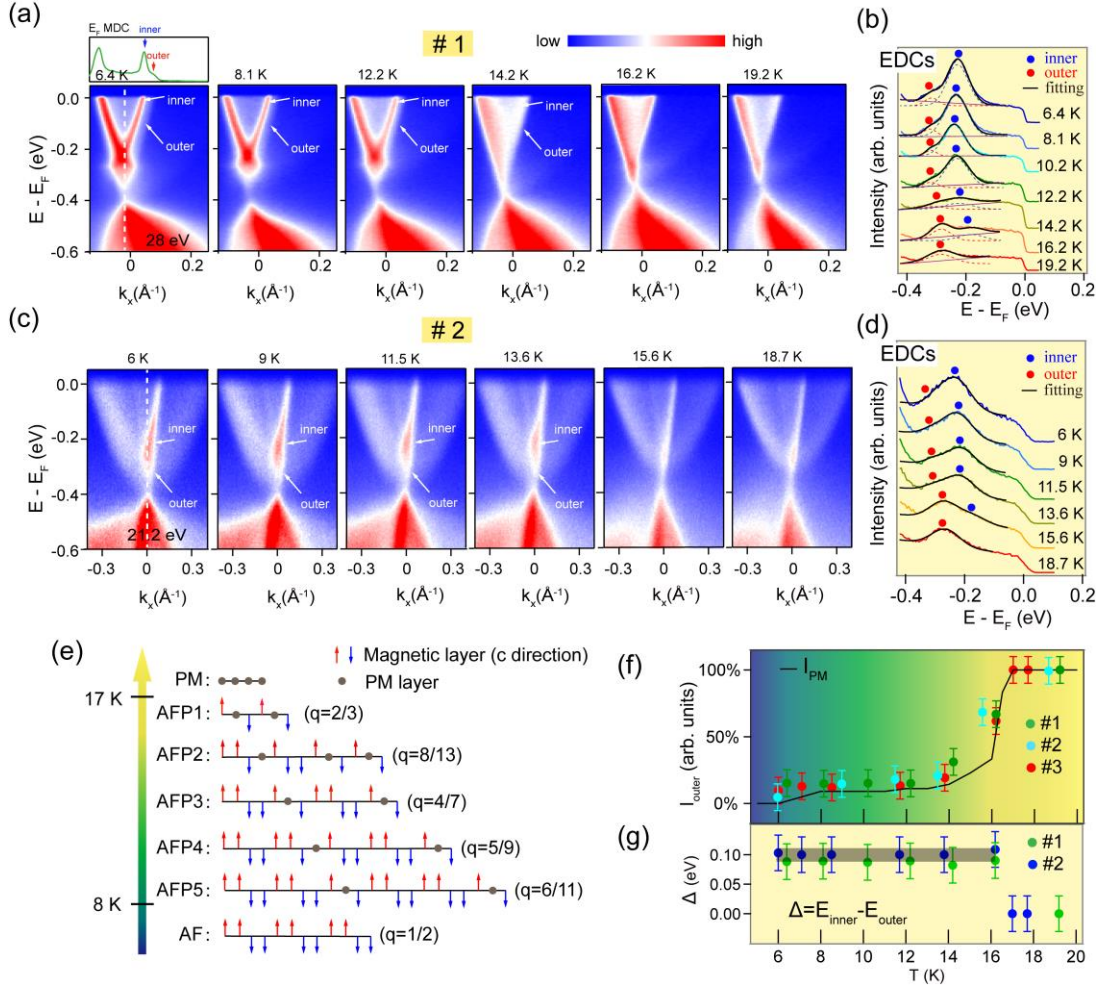


Fig. 4 Temperature dependence of the electron bands in the *ab*-domain. (a, c) Temperature-dependent ARPES spectra of the electron bands in the *ab*-domain, obtained using 28 eV and 21.2 eV photons, respectively. (b, d) Energy distribution curves (EDCs) extracted from a and c along the white dashed lines, respectively, with offset for clarity. Black lines represent fits to the EDC peaks. Red and blue dots indicate the peak positions of the outer and inner bands, respectively. Purple lines in b indicate the background distribution. (e) Schematic illustration of the devil's staircase. (f) Temperature dependence of the relative intensity of the outer bands ($I_{outer} = \text{outer}/(\text{inner} + \text{outer})$) from three different samples. The calculated occupancy of the paramagnetic layers (I_{PM}), derived from the DFT+U calculations based on the devil's staircase model, is shown for comparison. (g) Temperature dependence of the energy separation between the inner and outer bands.